AFRL-AFOSR-JP-TR-2018-0046

Investigations of magnetodielectric properties of multi-ferroic nanoparticle composite metamaterials

Yuanzhe Piao
SEOUL NATIONAL UNIVERSITY

04/17/2018
Final Report

Air Force Research Laboratory
AF Office Of Scientific Research (AFOSR)/ IOA
Arlington, Virginia 22203
Air Force Materiel Command

FORM SF 298

REPORT DOCUMENTATION PAGE

Form Approved
OMB No. 0704-0188

1. REPORT DATE *(DD-MM-YYYY)*	2. REPORT TYPE	3. DATES COVERED *(From - To)*
24-05-2018	Final	29 Sep 2015 to 28 Mar 2017

4. TITLE AND SUBTITLE
Investigations of magnetodielectric properties of multi-ferroic nanoparticle composite metamaterials

5a. CONTRACT NUMBER

5b. GRANT NUMBER
FA2386-15-1-4112

5c. PROGRAM ELEMENT NUMBER
61102F

6. AUTHOR(S)
Yuanzhe Piao, Peter Kofinas, Sylvie Begin-Colin

5d. PROJECT NUMBER

5e. TASK NUMBER

5f. WORK UNIT NUMBER

7. PERFORMING ORGANIZATION NAME(S) AND ADDRESS(ES)
SEOUL NATIONAL UNIVERSITY
SNUR&DB FOUNDATION RESEARCH PARK CENTER
SEOUL, 151742 KR

8. PERFORMING ORGANIZATION REPORT NUMBER

9. SPONSORING/MONITORING AGENCY NAME(S) AND ADDRESS(ES)
AOARD
UNIT 45002
APO AP 96338-5002

10. SPONSOR/MONITOR'S ACRONYM(S)
AFRL/AFOSR IOA

11. SPONSOR/MONITOR'S REPORT NUMBER(S)
AFRL-AFOSR-JP-TR-2018-0046

12. DISTRIBUTION/AVAILABILITY STATEMENT
A DISTRIBUTION UNLIMITED: PB Public Release

13. SUPPLEMENTARY NOTES

14. ABSTRACT
The French group of S. Begin has developed the synthesis and the structural and magnetic characterizations of these raspberry nanostructures in this AOARD project. Dr Yuangzhe Piao at Seoul National University, Seoul, Korea, has developed the synthesis of silica coated magnetite nanoparticles with regular magnetic properties. Professor Kofinas at the University of Maryland, College Park, MD, has developed the fabrication/characterization of flexible magnetodielectric composites using the aforementioned magnetite nano-objects.

15. SUBJECT TERMS
magnetodielectric, multi-ferroic nanoparticles, polymeric matrix

16. SECURITY CLASSIFICATION OF:			17. LIMITATION OF ABSTRACT	18. NUMBER OF PAGES	19a. NAME OF RESPONSIBLE PERSON
a. REPORT	b. ABSTRACT	c. THIS PAGE			KNOPP, JEREMY
Unclassified	Unclassified	Unclassified	SAR	23	19b. TELEPHONE NUMBER *(Include area code)* 315-227-7006

Multi-Ferroic Polymer Nanoparticle Composites for Next Generation Metamaterials

AWARD NO. FA2386-15-1-4112

Final Report – Sylvie Begin-Colin, CNRS-UDS, France

Peter Kofinas, University of Maryland, USA

Yuanzhe Piao, Seoul National University

Researchers involved in this project :
Peter Kofinas, University of Maryland, USA, kofinas@umd.edu
Sylvie Begin-Colin, CNRS-UDS, France, sylvie.begin@unistra.fr
Yuanzhe Piao, Seoul National University, Korea, parkat9@snu.ac.kr

Introduction

The aim of this project was the development of magnetodielectric polymer composites consisting of magnetic nanoparticles that posses high permeability (μ), permittivity (ε) and minimal dielectric and magnetic loss (tan δ). Materials with high dielectric constant (ε) and permeability (μ) are appealing for the development of microwave communications devices. Polymer based composite materials that possess high ε and μ are receiving a lot of interest recently, due to their malleability, low weight, and elastic properties. It is important however to note that conventional ferrite-polymer composites are limited to operating frequencies much lower than 1 GHz since their μ values decay rapidly beyond their resonance frequency (f_{res}). The best known examples are MnZn and NiZn ferrites which exhibit a f_{res} of 2MHz and 200MHz, respectively. Ferrites, particularly magnetite, have low saturation magnetization (M_s) by comparison to metals, which limits the product of μ and f_{res} as estimated via the Snoek limit. Thus, it is extremely difficult to obtain composites with high μ values at high operational frequencies using ferrites nanoparticles. However it has been recently demonstrated that it is possible to enhance the limited magnetic properties of magnetite nanoparticles by synthesizing nanostructures consisting of oriented aggregates of ferrite nanocrystals. These nanostructures also termed *raspberry nanostructures* consist of nanocystals with common crystallographic orientations directly combined together to form larger ones, which leads to magnetic collective assembly properties.

The french group of S. Begin has developped the synthesis and the structural and magnetic characterisations of these *raspberry nanostructures* in this AOARD project. Dr Yuangzhe Piao at Seoul National University, Seoul, Korea, has developped the synthesis of silica coated magnetite nanoparticles with regular magnetic properties. Professor Kofinas at the University of Maryland, College Park, MD, has developed the fabrication/characterization of flexible magnetodielectric composites using the aforementioned magnetite nano-objects.

Abstract : Design and characterizations of raspberry shaped nanostructures for flexible magnetodielectric composites and magnetically recoverable photocatalyst

Traditional magnetite nanoparticles have a saturation magnetization between 45 emu/g and 55 emu/g due to surface and volume spin canting and defects. However, it has been recently demonstrated that it is possible to improve the saturation magnetization of magnetite nanoparticles by their collective oriented organization in a single nanostructure. The research group of Pr. Sylvie Begin-Colin at IPCMS has synthesized corona shaped magnetite nanostructures that acquire collective assembly during synthesis. These nanostructures displaying a "raspberry" morphology have been synthesized by a solvo-thermal method adapted from Cheng et al. [*J. Chen et al. Adv. Mater. 17, (2005), 582-586*]. Nanostructures consist of spherical aggregates of small nanocrystals that exhibit hollow structures. The nanostructure size may be tuned in the range of 100 - 500 nm, and the nanocrystal sizes are modulated between 2 nm and 30 nm. These different nanostructures obtained by varying the reaction conditions (reaction time, reactants concentration) have been carefully characterized by different techniques such as HR-TEM, 3D tomography, SEM, BET, TGA, XRD, etc. Furthermore, the different reaction steps occurring during the synthesis have been investigated more intensively by following the temperature and pressure evolutions inside an instrumented autoclave. To produce larger amount of raspeberry shaped nanostructures (RSNs) necessary for magneto dielectric measurements, another bigger autoclave has been built and allowed producing 20h/batch. It has allowed providing the large amount of nanostructures to perform measurements at various frequencies. This synthesis part has led to a paper which should be submitted before june 2016, entitled "Formation Mechanism of Iron Oxide Raspberry Shaped Nanostructures" by Olivier Gerber, Benoit P. Pichon, Dris Ihawakrim, Ileana Florea, Simona Moldovan, Ovidiu Ersen, Dominique Begin, Jean-Marc Grenèche, Sebastien Lemonnier, Elodie Barraud, Sylvie Begin-Colin.

Two types of corona magnetite nanostructures with a mean size of 250 nm consisting of an orientated assembly of smaller magnetite nanoparticles with sizes either of 5 nm or 25 nm have been selected for the fabrication of flexible magnetodielectric composites by Professor Kofinas. First experiments have been performed with as synthesized RSNs by Pr Peter Kofinas but the dispersion of RSNS in the polymer matrix was not optimal. Therefore other batches of RSNs have been synthesized and citrated before sending them to Pr Kofinas. These citrated nanostructures, which are monocrystalline due to an oriented aggregation induced by the synthesis process, have achieved saturation magnetization values of 74 emu/g and 88 emu/g, respectively. Another important magnetic aspect of such RSNs is their infinitesimally small coercivity. Such magnetic nanostructures with high saturation magnetization and low levels of coercivity were shown to be promising candidates for magnetic fillers to fabricate high performance flexible magnetodielectric composites. This part has led to a published paper in J. Mater. Chem. C, 2016, 4, 2345 entitled "Stretchable Magneto-dielectric Composites Based on Raspberry-Shaped Iron Oxide Nanostructures" by Mert Vural, Olivier Gerber, Benoit P. Pichon, Sebastien Lemonnier, Elodie Barraud, Leo C. Kempel, Sylvie Begin-Colin and Peter Kofinas. The research of magnetically recoverable photocatalyst prepared by supporting TiO_2 nanoparticles on RSNs core@fibrous silica shell nanocomposite has led to a published paper in RSC Advances, 2017, 7, 9587 entitled "A magnetically recoverable photocatalyst prepared by supporting TiO_2 nanoparticles on a superparamagnetic iron oxide nanocluster core@fibrous silica shell nanocomposite" by Bokyung Seo, Chaedong Lee, Donggeon Yoo, Peter Kofinas and Yuanzhe Piao.

Report :

1. Synthesis mechanism of raspberry shaped nanostructures.

Iron oxide porous nanostructures have been synthesized by a modified polyol solvothermal approach involving iron chloride hexahydrate, urea, ethylenglycol and succinic acid as reactants. When the reaction is performed for 13 h under solvothermal conditions in a Teflon lined autoclave at 200 °C, a black powder is obtained which is washed successively with water and ethanol. SEM micrograph showed particles featured by a spherical shape and a size distribution centered to 250 nm (Figure 1a). They consist in aggregates of nanograins of 25 nm as shown by TEM micrographs (Figure 1b). Nanostructures are mainly constituted in the magnetite phase (a= 8.39(7) Å to compare to that of stoechiometric magnetite a= 8.396 Å (magnetite JCPDS file 19-629) and 70% of magnetite from Mössbauer spectra) (Figure 1f) and are featured by similar crystal orientation. Their saturation magnetisation is about 81 emu/g, larger than that of individual 25 nm sized iron oxide NPs. Furthermore, SEM micrographs showed some cavity of about 90 nm in broken RSNs which corresponds to a hollow structure (Figure 1d). It was confirmed by studying the cross-section of these objects after their embedding in a resin followed by a polishing step (Figure 1e).

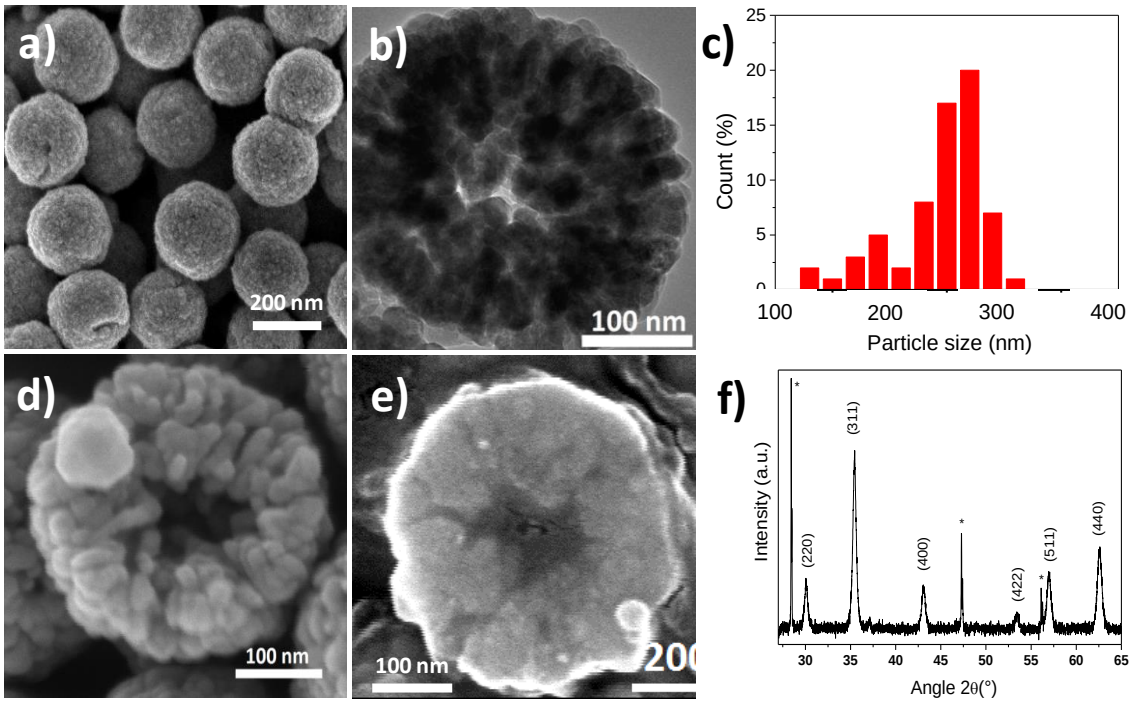

Figure 1. RSNs obtained after 13 h of reaction. a) SEM micrograph. b) TEM micrograph. c) Size distribution. SEM images on d) broken RSN and e) on the cross-section after embedding in a resin matrix and polishing. f) XRD pattern, stars correspond to silicon which used as a reference.

For a better understanding of the reaction mechanism, a time-resolved study has been performed by SEM on samples collected after different reaction times (Figure 2 and schema 1). After 4 hours of reaction, a gel-like structure with non-regular shape grains has been observed (Figure 2a), which is amorphous according to XRD analysis (not shown). FTIR spectrum exhibits νFe-O and νC-H bands at 500 cm^{-1} and 2900 cm^{-1}, respectively which suggests the formation of

an iron oxide based complex. After 5 h, the amorphous compound is no longer present and rather plate-like structures (PLS) with irregular morphologies (Figure 2b) and some small RSNs (with a mean size of about 100 nm) were observed (Figure S3 mais qui devient S2). After 6 h, RSNs are exclusively observed and are featured by a rather large bimodal size distribution with two main sizes centered to 90 nm and 200 nm with a heterogeneous nanograin (NG) size around 3-5 nm (Figure 2c). The mean RSN size get quite homogeneous after 7 h with a mean size of 250 nm with dispersion from 50 to 70 nm and then does not increase with reaction time. In contrast, the NG size increases gradually with the reaction time (up to 13 h). The porous structure has been also investigated by performing nitrogen absorption-desorption measurements (Table 1). Specific surface areas were estimated by the Brunauer-Emmett-Teller model and decrease gradually when reaction time increases which is in agreement with the increase in the NG sizes. After 9 hours of reaction, the formation of a cavity is observed. The increase of grain size may be correlated to the formation of cavities in RSNs since, given the experimental conditions, longer reaction times favor inside-out (or inverse) Ostwald ripening. The inner part of RSNs solubilizes and recristalizes onto grains located at the surface of RSNs. The observed synthesis pathway is described in Schema 1. To better understand the synthesis mechanisms, the PLS have been deeply investigated.

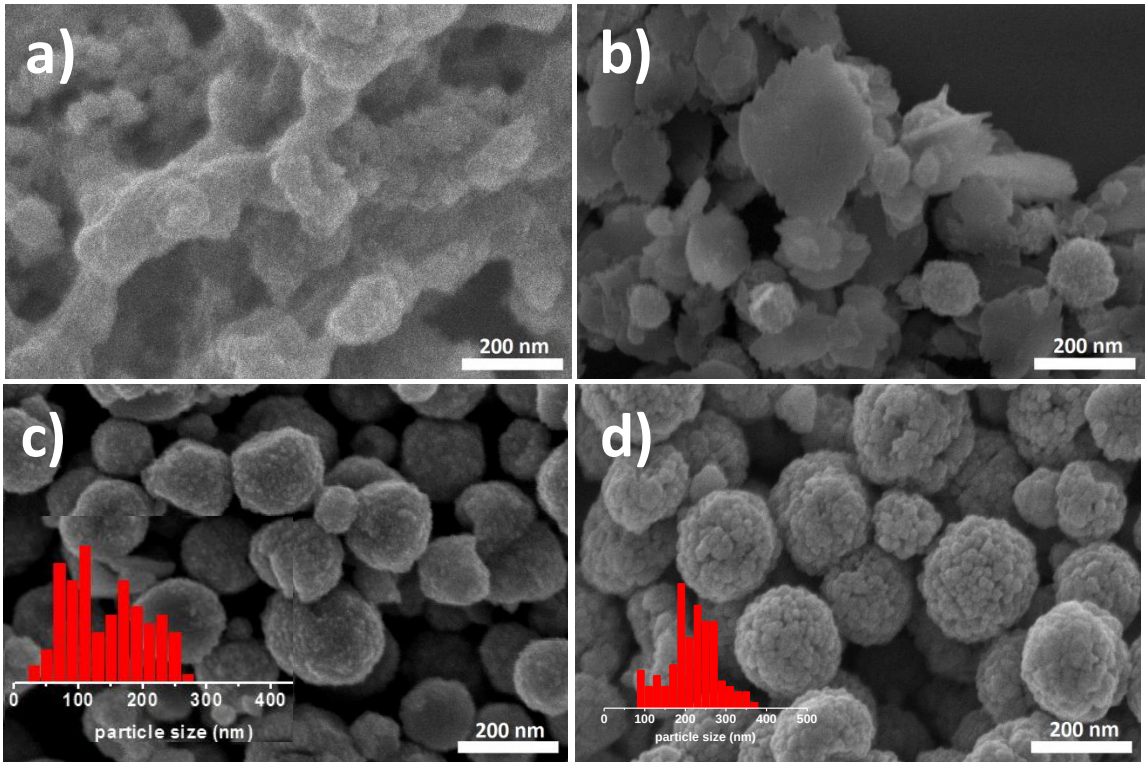

Figure 2. SEM micrographs corresponding to samples collected after a) 4 h, b) 5 h, c) 6 h and d) 9 h of reaction. Insets correspond to the size distribution measured from SEM micrographs.

Table 1. Structural caracteristics of raspberry-shaped nanostructures.

Reaction time	RSN size (nm)	Nanograin size (nm)	Surface specific area (m^2/g)
6h	90 & 200 ± 10	5 ± 3	61
7h	250 ± 50	5 ± 2	57
9h	250 ± 30	12 ± 2	38
12h	250 ± 12	25 ± 3	27

The intermediate formation of PLS is rather surprising and, to the best of our knowledge, has not been reported yet as an intermediate compounds in the synthesis of iron oxide nanocrystal clusters by the polyol solvothermal method. As they appear as key step in the synthesis process, their structure has been deeply investigated by TEM, TGA, IR and in situ TEM studies in temperature. This study is detailled in the paper to be submitted.

Discussion - reaction mechanism

The formation of RSNs is rather complex since the reaction proceeds through a multistep process (Scheme 1). The observation of the RSN synthesis at different reaction times has shown that an amorphous phase is formed after 4 hours and after 5 hours, small RSNs are observed together with PLS. When the reaction time increases, the PLS disppear simultaneously with the observation of a growth in the mean size of RSN (the NG size staying similar) which stabilizes after 7h of reaction. From 7h of reaction, the increase in the reaction time does not modify the mean size of RSNs while the mean size of NG increases and a core cavity forms.

Schema 1. Schematic representation of the synthesis pathway.

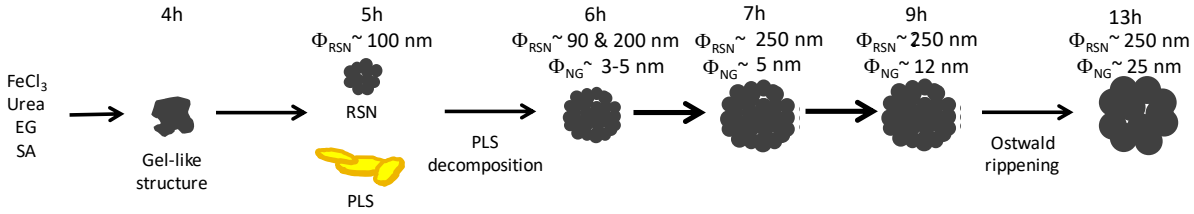

The temperature and pressure have been recorded during the synthesis (Figure 3) in order to get a better understanding on the reaction mechanism. One may first notice that after 4h hours of reaction, the temperature and pressure are stabilized and the observed phases are thus formed in similar conditions of pressure and temperatures. An increase of pressure is observed after 2,5 h and is directly correlated to the endothermic peak at 130 °C in the temperature curve. These features correspond to the decomposition of urea in ammoniac which is catalyzed by hexahydrate Fe(III) chlorides. Indeed they are not observed when heating the reaction medium without using $FeCl_3.6H_2O$ (Figure 3). Then ammonia reacts with water molecules leading to the formation of OH^- + NH_4^+. These conditions (increases the alkalanity of the reaction media and presence of hydroxides) are well known to favor the co-precipitation of iron oxide NGs from intermediate iron hydroxides. That would explain the observation of small RSNs after 5 h of reaction.

However an amorphous phase is observed before at 4h and may be due to competitive interactions. Indeed when urea decomposes in ammoniac, alkaline conditions favor also the deprotonation of ethylene glycol which coordinate with Fe species. Therefore one may suggest that the amorphous phase observed after 4 h of reaction results from the competitive interaction of ammonia with water and EG leading thus to amorphous intermediate alkoxide and iron hydroxyde phases.

After 4 hours, the temperature and pressure reach their maximum and favor the formation of plate-like structures resulting from interaction of iron cations with OH- and deprotonated ethylen glycol and the coprecipitation of smal iron oxide NGs. The reaction conditions favor the agregation of these NGs in nanostructures. The thermal studies performed on PLS have shown that these PLS are thermallly stable at high temperature which explains that they are identified and also may be easily extracted from the reaction media after 4 h of reaction. Besides some PLS may be shown to be incorporated in RSNs. However at 4 h, the maximum temperature and pressure are reached and the PLS begin to decomposes. PLS acts as an intermediate iron precursor (or iron reservoir) which decomposes at higher temperature and should induce heterogeneous nucleation of nanocrystals on previously formed iron oxide based RSNs. This would explain the increase of the mean RSNs size when that of NGs stays quite constant between 4 and 7 hours of reaction.

Such heterogeneous nucleation should favor the oriented agregation of NGs which is emphasized by the high pressure and temperature conditions which lead to well-shaped RSNs with narrow size distribution after 7 h of reaction. From 7h, there are no more iron precursors available in the media and RSNs reach their maximum sizes. As the reaction time increases in these high pressure and temperature conditions, digestive inside-out Ostwald ripening proceeds to solubilization-recrystallization of grains. Nanograins located at the center of RSNs undergo solubilization while the ones located close to the surface grow with the reaction time.

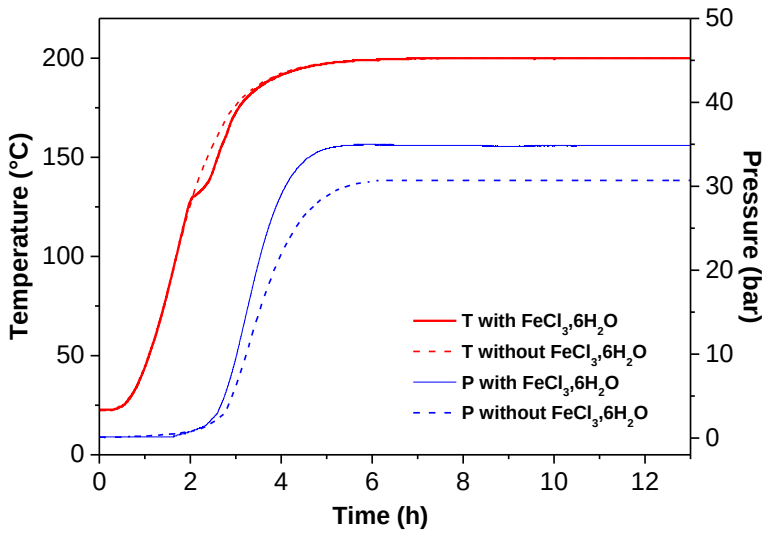

Figure 3. Temperature and pressure measurements as function of reaction time with (solid line) and without (dot line) iron chloride precursor.

Conclusion : The mechanism formation of porous raspberry shaped nanostructures synthesized by a one-pot polyol solvothermal method has been investigated in details from the early stages by using a combination of a wide panel of characterization techniques, namely SEM, TEM, XRD, FTIR spectroscopy, Mössbauer spectroscopy, elemental analysis, EELS and thermogravimetric analysis. A time resolved study demonstrates the intermediate formation of an amorphous iron alkoxide phase with a plate-like lamellar (PLS) structure. We showed thus that the synthesis of RSNs involved two iron precursors : the starting one and this in-situ formed iron alkoxide precursor which decomposes with time and heating and contributes to the growth step of nanostructures. Finally, a formation mechanism of RSN from such an original PLS structure, which is commonly admitted to proceed through the oriented aggregation of nanocrystals, has been proposed. Such a study will allow to propose strategies to dope these RSNs with other elements such as Mn, Co, Ni or Zn to improve their magnetic properties.

2. Design and structural and magnetic characterizations of citrated raspberry nanostructures for the fabrication of stretchable magneto-dielectric composites.

The iron oxide RSNs have been synthesized by a one-pot modified polyol solvothermal method. The reaction time may be used to alter the structure, composition and magnetic properties of the filler iron oxide RSNs (see § above). The solvothermal syntheses with reaction periods of 7 and 13 hours, result in spherical hollow clusters with a similar mean size around 250 nm and constituted of iron oxide nanocrystals with a mean nanocrystal size of 5 and 25 nm, respectively. These two types of RSNs have been selected for the fabrication of stretchable magneto-dielectric composites. However to favor their dispersion in polymer matrix, these RSNs have been citrated and their characterization is detailled below.

The structure of the RSNs fillers prepared using two reaction durations was characterized with X-Ray diffraction, Mössbauer spectroscopy and electron microscopies. The scanning electron microscopy (SEM) images revealed that both RSN fillers have an average diameter of about 250 nm (Figure 4 a, d). The surface roughness apparent in SEM images is indicative of a cluster-like structure. The transmission electron microscopy (TEM) characterization has demonstrated that these nanoclusters possess a hollow core, which validates the raspberry-like shape of this filler material (Figure 4a-inset, d, e). High-resolution TEM (HRTEM) images of the interface between two crystals in these RSN filler materials (Figure 5) and selected area electron diffraction (SAED) patterns (Figure 4c, f) confirm the oriented attachment of nanocrystals in RSNs. Indeed the HRTEM images clearly demonstrate that crystallographic orientations of nanocrystals are matched at the interface, which is indicative of a common crystal orientation shared by nanocrystals forming the RSN fillers (Figure 5). SAED patterns verified the formation of the spinel phase (Figure 4 c, e) and are consistent with single crystal structures (SAED patterns on single RSNs show Von Laue patterns instead of Debye rings). These observations show that RSNs are constituted of aggregated nanocrystals, which have similar crystallographic orientations.

The detailed characterization of the RSNs microstructure has showed that RSN fillers allowed to react for 7 hours (RSN5) have finer nanocrystal size than fillers allowed to react for 13 hours (RSN25) (Figure 4). From TEM micrographs, a mean nanocrystal size of 5 and 25 nm is determined for RSN5 and RSN25 respectively while crystallite sizes calculated from Rietveld analysis of X-Ray Diffraction (XRD) patterns (Figure 5b) are respectively 14 ± 1 and 15 ± 1 nm.

Such discrepancies between both measurements were related to the monocrystalline nature of the RSNs and the presence of defects or dislocation induced during the synthesis process. Indeed SAED patterns (Figure 4.c,f) and HRTEM of nanocrystal interfaces (Figure 5a) confirms the monocrystalline structure of RSNs, which is established with aggregates of nanocrystals with similar crystal orientations. However, the extended Von Laue spots in SAED patterns evidenced a slight misalignment in the orientation of these nanocrystals. In addition, Fast Fourier Transform (FFT) analysis performed on SAED patterns of RSNs has demonstrated the presence of defects.

XRD patterns of RSNs display characteristic peaks of the iron oxide spinel structure (Figure 5b). Lattice parameter deduced from XRD pattern is very close to that of stoichiometric magnetite for RSN25 and indicates an oxidized state for RSN5. In addition, Mössbauer spectroscopy confirmed that RSN fillers with smaller crystal size have a maghemite-rich composition ($Fe_{2.78}O_4$, 70% of maghemite) while those with large crystal size are mainly constituted of magnetite Fe_3O_4 phase ($Fe_{2.90}O_4$, 70% of magnetite). These variations in composition is explained by the surface oxidation of magnetite, which might be elevated due to smaller crystal size of maghemite-rich RSN fillers.

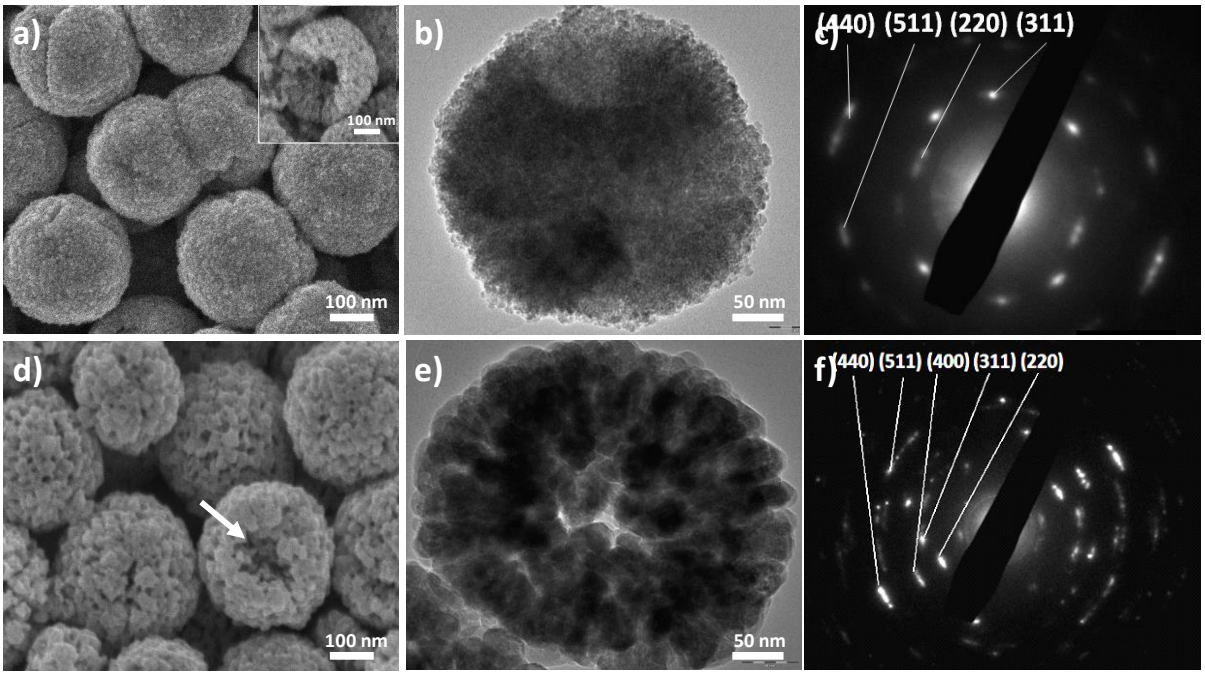

Figure 4. SEM images of citrate-capped RSNs reacted for (a) 7 hours, and (b) 13 hours. TEM images of citrate-capped RSNs reacted for (d) 7 hours, and (e) 13 hours. SAED patterns of citrate-capped RSNs reacted for (c) 7 hours, and (f) 13 hours.

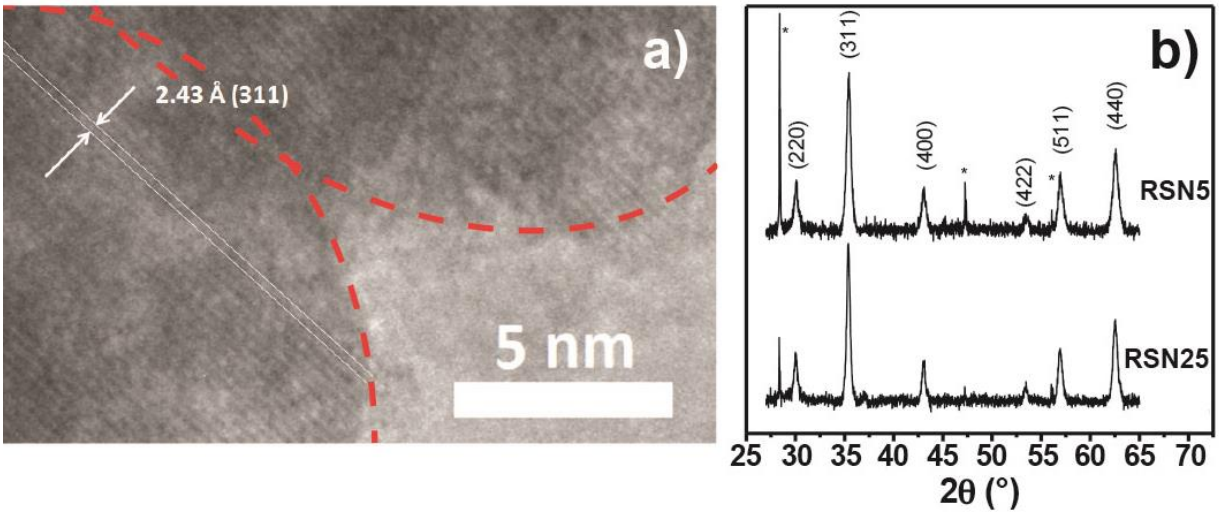

Figure 5. (a) HRTEM image of RSNs which shows on the nanostructure border that several nanocrystals display the same crystalline orientation. (b) XRD data for RSN5 and RSN25.

The characterization of the magnetic properties of RSN fillers correlates well with their structure and composition. The RSNs are superparamagnetic at 300K as the coercivity of both magnetite- and maghemite-rich RSNs at 5K remains below 300 Oe (Figure 6-insets), which is indicative of small nanocrystal size. The citrated RSN25 have demonstrated a M_s of 88 emu/g, which is comparable to the bulk M_s of magnetite (92 emu/g) and that of RSN5 is around 74 emu/g which is closed to bulk maghemite (Figure 6a,b). In contrast to RSNs, individual magnetite nanoparticles with a similar nanocrystal size have a saturation magnetization between 45 emu/g and 70 emu/g due to defects, surface and volume spin canting. In fact, the structuration of RSNs, which display aggregated orientation of nanocrystals has a critical role for improving the structural and magnetic order, limiting the influence of surface and volume spin canting. The strong dipolar interactions between nanocrystals forming RSNs favors the coupling of spins at the grain surface, which reduces the magnetic and structural disorder arising commonly from defects or broken bonds in the surface of iron oxide nanocrystals. Because of the strong dipolar interactions between nanocrystals, and the common crystallographic orientation of grains, RSNs exhibit higher crystal quality, and lower spin canting than individual iron oxide nanoparticles, which leads to magnetization values matching bulk materials.

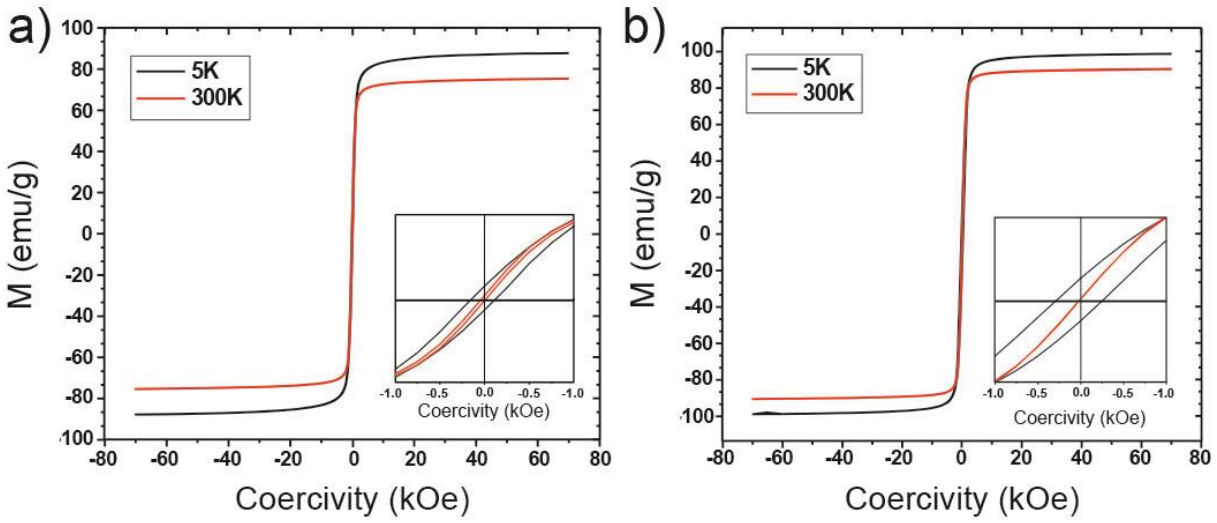

Figure 6. Magnetization curves for a) maghemite-rich (RSN5) and b) magnetite-rich (RSN25) RSNs at 5 K and 300K.

The influence of citrate capping on the surface charge of the RSNs was quantified using zeta potential experiments. The RSNs exhibited zeta potential values close to zero prior to attachment of the citrate capping agent, which is in agreement with the isoelectric point of iron oxide (IEP=6.8). The zeta potential of RSNs reached -56 mV with citrate capping, which results in better colloidal stability with the help of electrostatic interactions. These citrate-capped RSNs with a negative surface charge were easily dispersed in a polydimethylsiloxane (PDMS) elastomer matrix and cross-linked to form stretchable magneto-dielectric composites.

Conclusion. Stretchable magneto-dielectric composites were prepared using collectively assembled iron oxide nanostructures as fillers in an elastomer (polydimethylsiloxane) matrix. These raspberry-shaped nanostructures (RSNs), synthesized by a one-pot polyol solvothermal method, consist of oriented aggregates of iron oxide nanocrystals (nanocrystals with common crystallographic orientations directly combined together to form larger ones), which ensure a very low oxidation state of Fe_3-xO_4 nanocrystals and lead to interesting magnetic properties. The oriented aggregation of nanocrystals generates a large interface between nanograins significantly reducing their surface oxidation, improving crystal quality and preventing the formation of surface and volume spin canting. Therefore these iron oxide RSNs display low coercivity with enhanced saturation magnetization (M_s). The use of such citrated RSN as filler material with improved magnetization and low coercivity allowed the fabrication of magneto-dielectric composites that can combine permeability values reaching 2.3 with magnetic loss values limited to 0.11. The resulting composites can also be stretched up to 165% strain before failure due to good adhesion between the elastomer and citrate capped RSNs. In addition, the composition of these fillers was altered to adjust the resonance frequency of the resulting composite material. Stretchable magneto-dielectric composites consisting of maghemite-rich RSNs and magnetite-rich RSNs demonstrated resonance frequencies similar to the spherical ferrimagnetic/ferromagnetic resonance of maghemite and magnetite, respectively.

3. Magnetically recoverable photocatalyst prepared by supporting TiO_2 nanoparticles on a superparamagnetic raspberry shaped nanostructures iron oxide nanocluster core@fibrous silica shell nanocomposite

A magnetically recoverable photocatalyst was prepared by supporting TiO_2 nanoparticles on a superparamagnetic iron oxide nanocluster (SION) core@fibrous silica shell (FSS) nanocomposite. Using the raspberry-shaped magnetic iron oxide nanocluster core as a seed, FSS with uniform thickness was grown directly on the core surface by a sol-gel process. The preparation method was optimized to have a single core for each nanoparticle by adjusting the amount of the silica source. The FSS has a fanning structure of radial pores, which enable large amounts of TiO_2 nanoparticles to be supported easily on the pore surface. SION@FSS with amorphous TiO_2 loaded on the pores (SION@FSS@Am- TiO_2) was crystallized to the anatase phase (SION@FSS@A- TiO_2), which shows good photocatalytic effect. When used for water purification, SION@FSS@A- TiO_2 shows faster dye degradation kinetics than that of commercial P25 nanoparticles. The as-prepared SION@FSS@A- TiO_2 photocatalyst could be magnetically recovered easily from water after decolorization of dye.

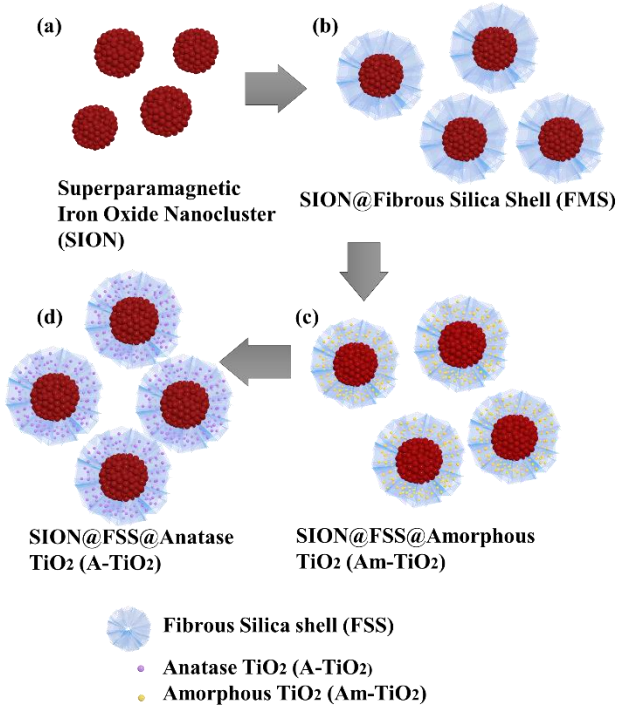

Scheme 1 Schematic of the procedure for preparing magnetically recoverable photocatalyst: (a) SION, (b) SION@FSS, (c) SION@FSS@Am-TiO_2 and (d) SION@FSS@A-TiO_2.

The procedure for the synthesis of SION@FSS@A-TiO_2 (**Scheme 1**) involves three steps. First, the SIONs are homogeneously coated with dendritic FSS by a sol-gel process[31]. Next, amorphous TiO_2 nanoparticles were deposited on the FSS to form SION@FSS@Am - TiO_2 , which undergo a hydrothermal reaction to yield the SION@FSS@A-TiO_2.

The starting SION has a raspberry-like shape4s, which is a conglobulation of 5–10-nm iron oxide nanocrystals packed into a 280 ± 37-nm nanoclusters. These SIONs combine

the advantages of individual grains and confer an enhanced magnetic property. The oil−water biphase stratification approach[31] was used to prepare a silica coating shell with fibrous large pores that enable enhanced adsorption and release ability. To generate such silica coating shells, SIONs were first dispersed in water and mixed with CTAB and TEA. Then, TEOS and 1-octadecene were added to the mixture; the mixture was hydrolyzed and condensed to generate the first FSS layer on SION. The second-layer generation step starts with discarding the oil layer and adding TEOS and decalin. The final layer is generated using a mixture of TEOS and cyclohexane as an oil-based solvent. After removing residual CTABs by calcination, TBOT was added dropwise to an ethanolic solution of SION@FSS and water. Amorphous TiO_2 nanoparticles supported on SION@FSS were crystallized using the hydrothermal method. EDX analysis shows that iron and oxide spectra are dominant in the center of the particles and silica and titanium spectra dominate on the outer side of the particles.

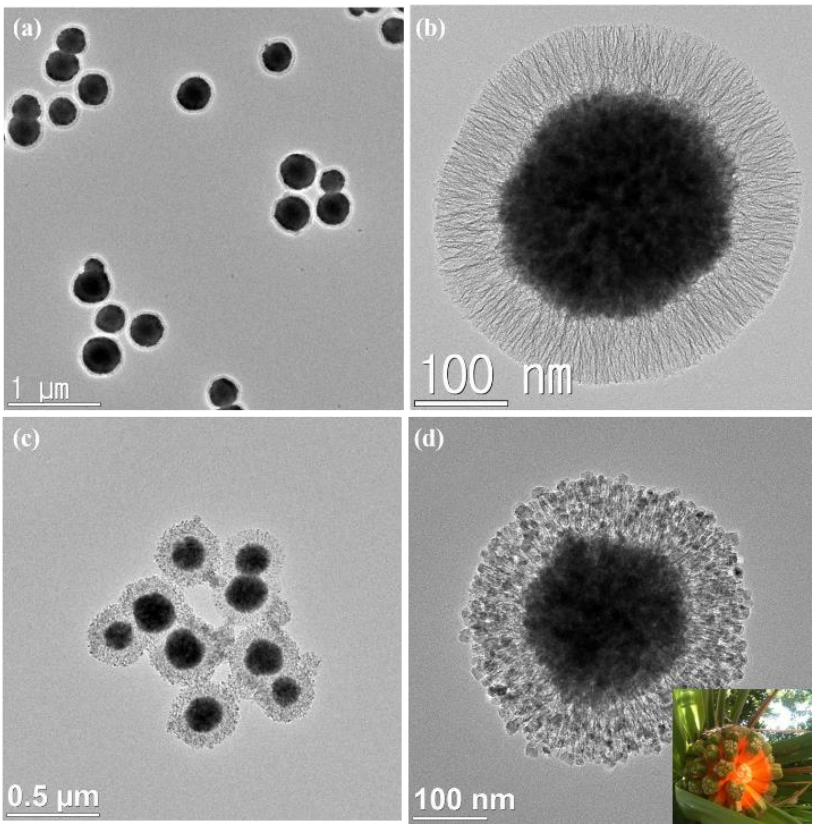

Figure 7. TEM images of SION@FSS at the end of the third layer growth (a, b) and SION@FSS@A-TiO_2 as a final product for water purification (c, d). Inset of (d) shows the picture of a screwpine which has a shape similar to that of SION@FSS@A-TiO_2

Fibrous silica shell with uniform layer thickness could be clearly seen in both TEM (**Figure 7**) and SEM images (**Figure 8**). Average size of SION@FSS was 317.7 ± 56.2 nm, as shown in the SEM images. The average layer thickness of SION@FSS was 71.1 ± 7.5 nm. SION@FSS shows wide size distribution owing to the polydispersity of the iron oxide cores, but the thickness of FSS is uniform irrespective of the size of the core. The size of prehydrothermal SION@FSS@Am - TiO_2 was 324 ± 50.0 nm and that of posthydrothermal SION@FSS@A-TiO_2 was 305 ± 37.9 nm, as derived from the SEM observations. The thickness of the coating FSS + Am-TiO_2 layer was 70.5 ± 9.1 nm. To

crystalize the TiO_2 nanoparticle from amorphous to anatase phase, hydrothermal method is used due to low energy required compared to high temperature furnace method. After the posthydrothermal treatment, the layer shrunk a little to 68.9 ± 8.3 nm. It has been reported that silica could be partially etched during the hydrothermal treatment.

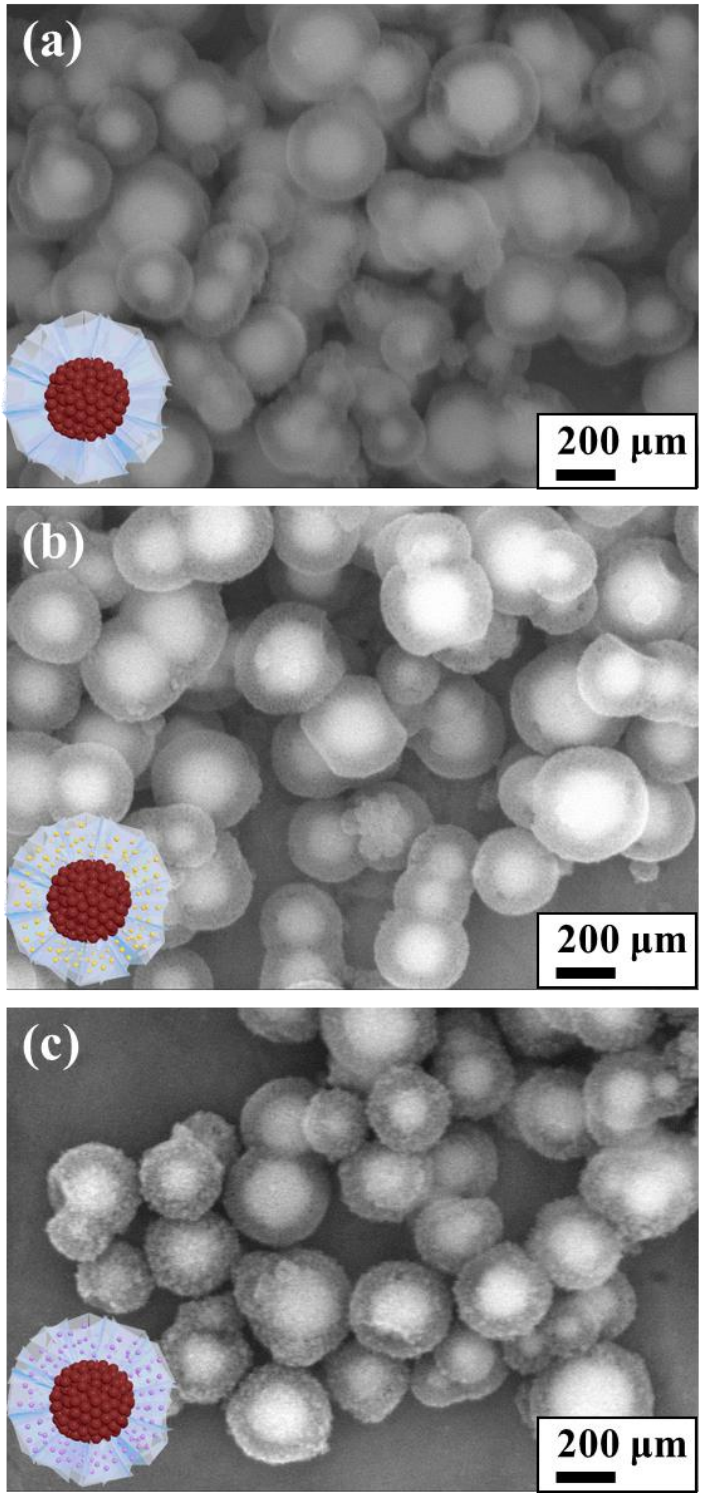

Figure 8. SEM images of (a) SION@FSS, (b) SION@FSS@Am-TiO_2 and (c) SION@FSS@A-TiO_2.

For SION@FSS synthesis without residual FSS particles, the amount of TEOS was adjusted from 4 ml to 12.5 µl during the first layer stratification. When 4 ml of TEOS was added, SION@FSS spheres were fused with several FSS particles. The aggregated FSS spheres were separated when the TEOS amount was reduced to 1 ml, but SION@FSS agglomerates were still present. Separation of fused SION@FSS was obtained by gradually reducing the TEOS volume to 250 µl. Fully separated SION@FSS nanoparticles started to appear on using 50 µl of TEOS. By reducing the TEOS volume below 50 µl, the FSS layer becomes thinner and cannot be observed by TEM. After first and second FSS were coated on single SION@FSS nanoparticles, TEOS volume was controlled for the third layer generation. Likewise, the amount of TEOS is optimized to have single core for each nanocomposites.

To take advantage of their wide surface area and application in photocatalysis, TiO_2 spheres were confined in pores. To increase the filling amount without remnant TiO_2 spheres, the amount of TBOT was adjusted from 10 µl to 2 ml. Experimental results showed that 400–800 µl of TBOT was sufficient to fill in the FSS pores. When the TBOT concentration reached 1% (v/v), fused SION@FSS@Am - TiO_2 nanoparticles were observed. Otherwise, when TBOT concentration was too low, considerable number of the FSS pores remained empty. As a result, SION@FSS@Am-TiO_2 synthesized with 800 µl of the titanium precursor was used for further analysis.

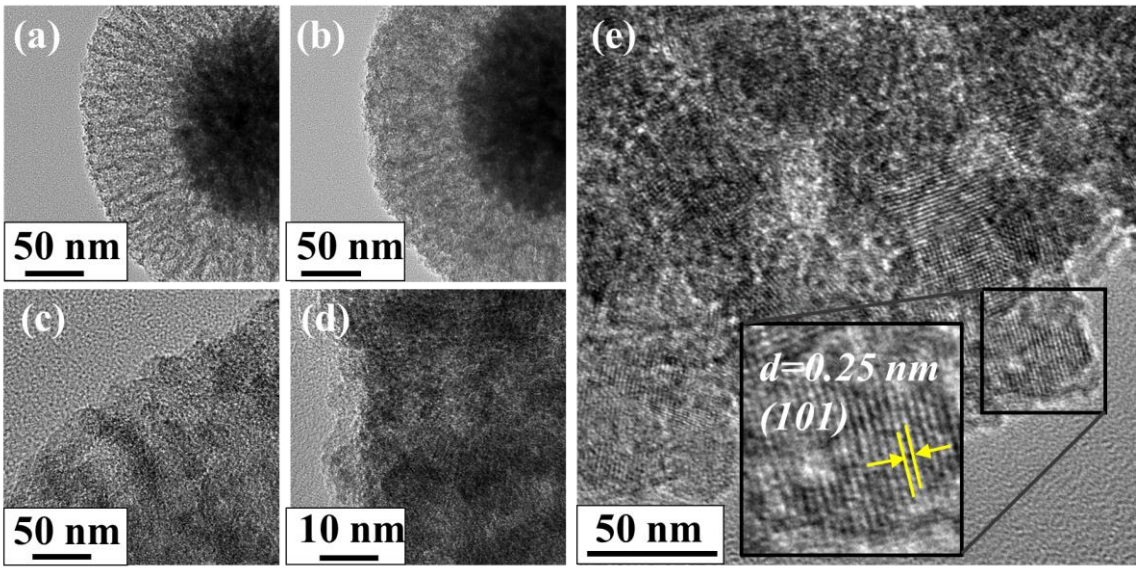

Figure 9. TEM images of IO@FSS@Am-TiO_2 showing Amorphous (a-d) to anatase phase transition of grafted titanium oxide nanoparticles. Lattice fringes correspond to (101) plane of anatase are found on IO@FSS@Am-TiO_2 (e). Amount of the TiO_2 precursor (TBOT) were adjusted to 400 µl ((a), (c) (magnified view)) and 800 µl ((b), (d) (magnified view)).

Titanium dioxide nanoparticle loading were verified from both TEM images (Error! Reference source not found.9) and EDX analysis. When 400 µl of TBOT was used (Error! Reference source not found., (a)), more pore voids between the FSS layers were observed compared to when 800 µl of TBOT was used (b). On magnified view (b, d), more TiO_2 nanoparticles were observed when 400 µl of TBOT was used (c) compared with that when 800 µl of TBOT (d). It shows high possibility of greater TiO_2 nanoparticles loading on

SION@FSS@Am-TiO_2 by increasing the amount of titanium precursor. Loading of TiO_2 nanoparticles after hydrothermal reaction was determined by the crystalline structure the grains observed between the FSS layers, which matches the (101) plane of the anatase nanocrystals (e).

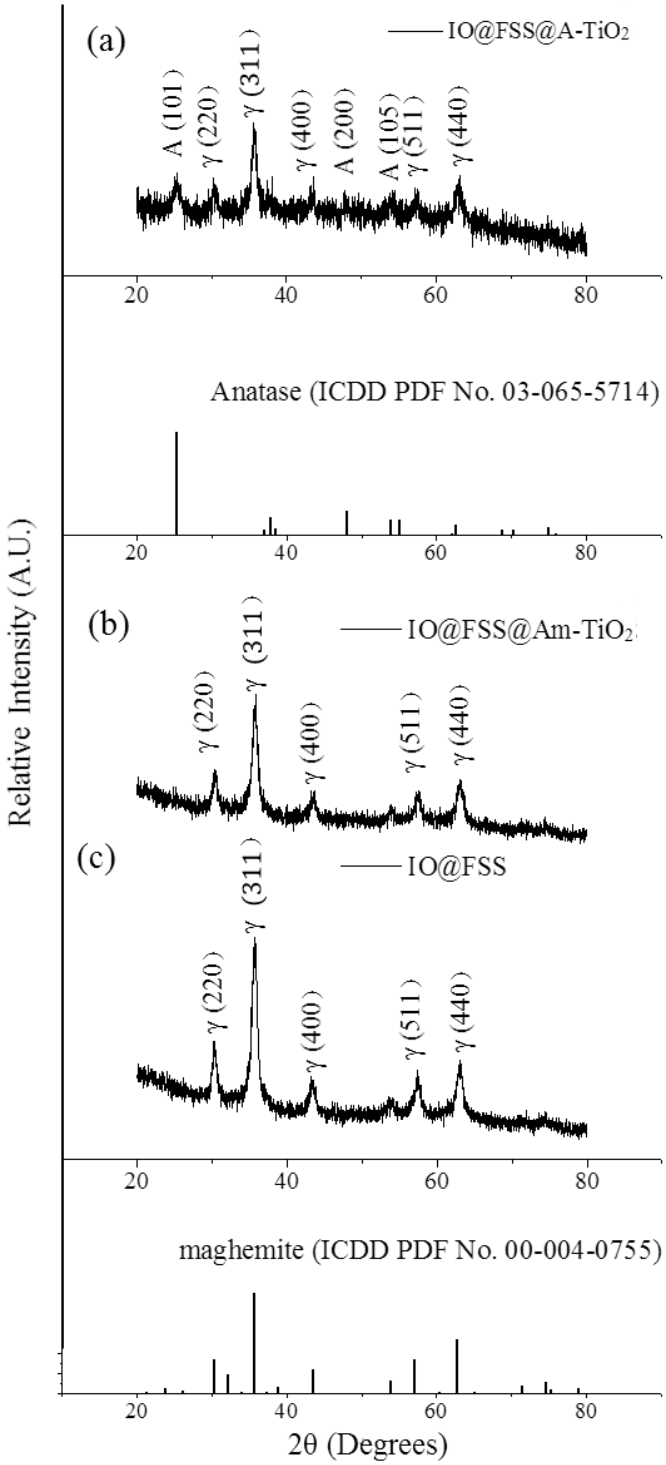

Figure 10. X-ray diffraction analysis of (a) SION@FSS@A-TiO_2, (b) SION@FSS@Am-TiO_2 and (c) SION@FSS. Crystal planes are indexed with γ (maghemite) and A (anatase).

Crystalline structures were investigated by powder X-ray diffraction (XRD) (Error! Reference source not found.). The grain size of SION was calculated by the Debye-Scherrer equation. Using the most intense diffraction peak from figure 4 (c), the (311) plane of maghemite, it was found that the SION has 10.94 nm grains. Since amorphous TiO_2 shows less photocatalytic activity compared to anatase TiO_2, the nanocomposite undergoes crystallization. The phases of the titanium-coated samples before and after the crystallization step were characterized (Error! Reference source not found.). Prehydrothermal TiO_2 nanoparticles were amorphous as no SION@FSS@Am - TiO_2 spectrum (b) matched that of anatase (ICDD PDF card 03-065-5714). Maghemite (ICDD PDF card 00-004-0755) peaks or patterns are dominant in both XRD (Error! Reference source not found.) and SAED (**Figure 11**) results, suggesting that the iron oxide core is maghemite in nature with polycrystalline structure. The core is initially magnetite, but undergoes transition to maghemite during the hydrothermal reaction. After the hydrothermal reaction, the diffraction spectrum obtained from SION@FSS@A - TiO_2 (Error! Reference source not found. (a)) shows a peak at 25.3˚ corresponding to the (101) reflection of anatase. Peaks at 48.04˚ and 53.88˚ are attributed to the (200) and (105) planes, respectively, of the anatase-phase TiO_2.

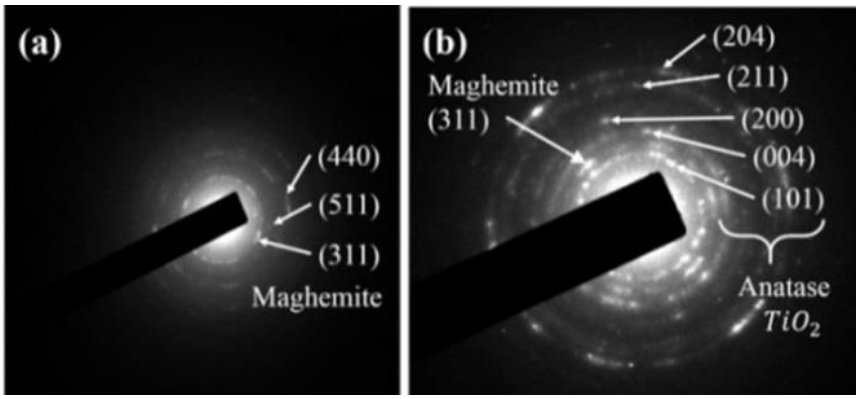

Figure 11. SAED patterns of (a) SION@FSS@Am-TiO_2 and (b) SION@FSS@A-TiO_2.

Although maghemite spectra are dominant in XRD, SAED analysis clearly revealed the existence of other anatase planes. The five ring patterns in (**Figure 11,** (b)) correspond to the (204), (211), (200), (004), and (101) planes of anatase TiO_2. The most intense peak of SION@FSS@A-TiO_2 in the SAED patterns corresponds to the (311) plane of maghemite. To sum up, appearance of anatase peaks prove the transition of amorphous to anatase phase of the supported TiO_2 after the hydrothermal treatment.

Table 1 Morphological and textural characteristics of the nanoparticles

Sample Name	S_{BET} (m^2/g)	V_t (cm^3/g)	D_{BJH} (nm)
SION@FSS	265.62	0.745	11.22
SION@FSS@Am-TiO_2	237.07	0.434	8.39
SION@FSS@A-TiO_2	149.98	0.434	12.77

S_{BET}, Brunauer-Emmett-Teller pore surface area (m^2/g). V_t, Single-point adsorption total pore volume at P/P_o=0.994; D_{BJH}, Barrett-Joyner-Halenda adsorption average pore diameter.

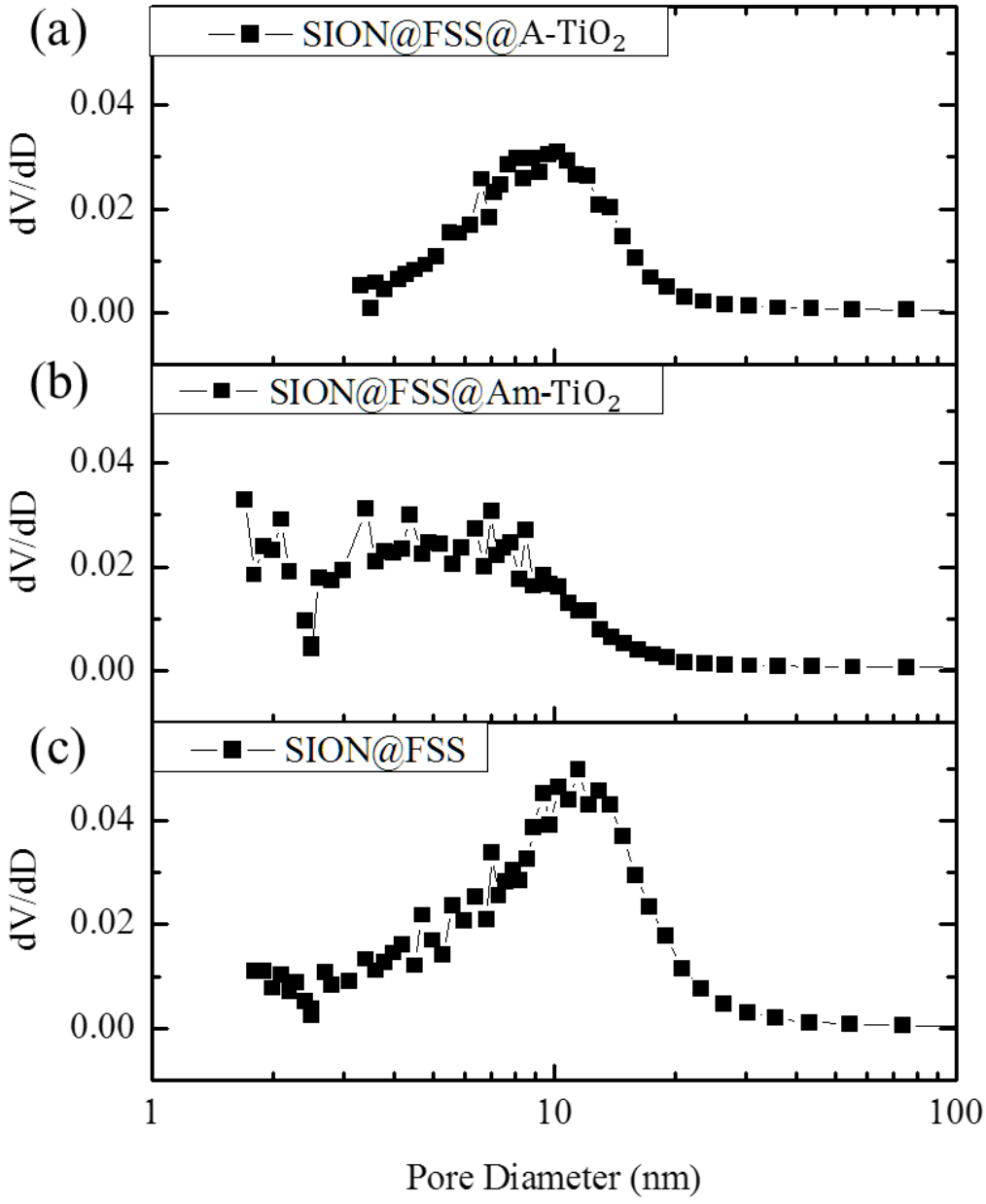

Figure 12. Pore size distributions of SION@FSS (a), SION@FSS@Am-TiO_2 (b) and SION@FSS@A-TiO_2 (c).

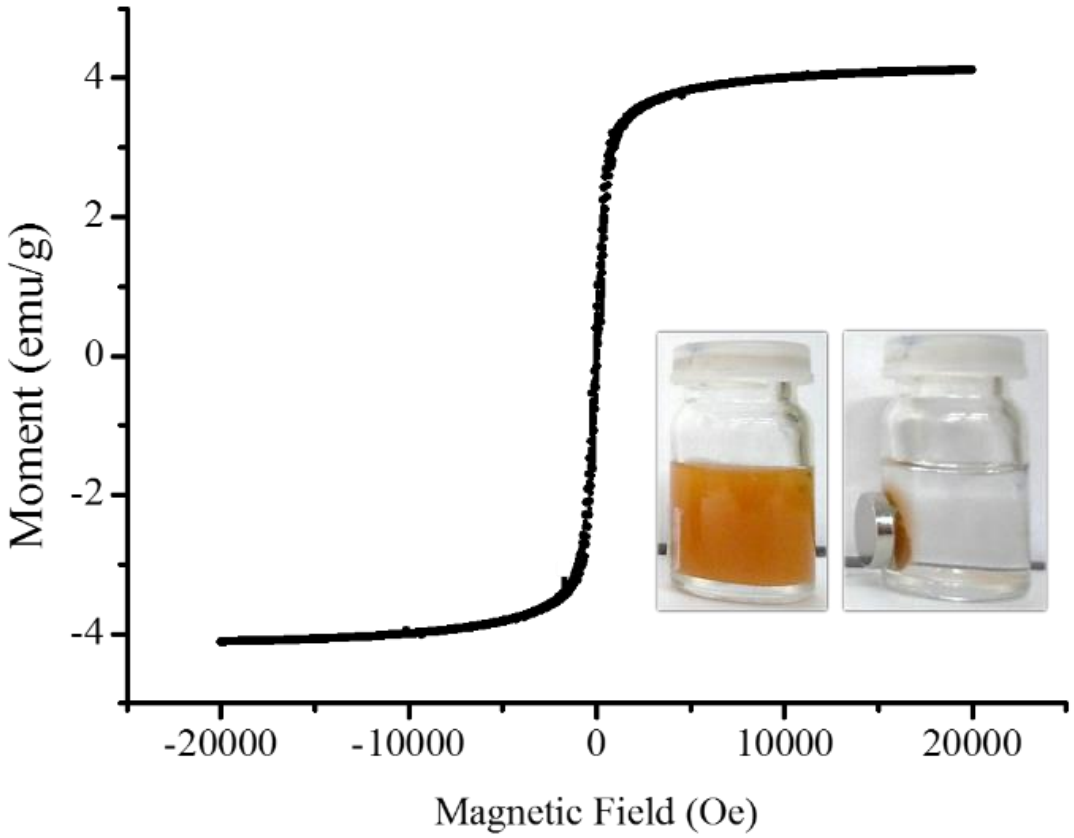

Figure 13. Field-dependence of magnetization graph of SION@FSS@A-TiO_2 measured at 20 K. Inset shows SION@FSS@A-TiO_2 dispersed in ethanol (left) and magnetically collected SION@FSS@A-TiO_2 (right).

Morphological change at each synthesis step is summarized in the

Table 1. Total pore volume of the SION@FSS spheres, 0.745 cm^3/g, match that of the FSS spheres from the previous report, 0.689 cm^3 /g. Reduced surface area of SION@FSS@Am-TiO_2 confirms that TiO_2 is supported in the SION@FSS pores. During the hydrothermal reaction, amorphous TiO_2 undergoes crystallization and crystal growth, leading to the increased TiO_2 nanoparticle size. Thus, pores below 10 nm are absent from the pore size distribution graph of SION@FSS@A-TiO_2 (Error! Reference source not found.). Therefore, increased pore size after hydrothermal reaction is expected to be due to the removal of micropores and mesopores from between the TiO_2 nanoparticles[53]. This also leads to close packing of the TiO_2 nanoparticles, which reduces the SION@FSS@A-TiO_2 surface area to 149.98 m^2/g.

The nanoparticles were recollected using the magnetic property of the iron oxide core. The graph of induced magnetization versus field shows saturation magnetization at 4.114 emu/g (Error! Reference source not found.). Saturation magnetization of SION@FSS@Am-TiO_2 is lower than that of the iron oxide core, owing to the presence of silica and TiO_2 nanoparticle that do not contribute to magnetic induction. In addition, the combined effect may be integrated with the reduced magnetization value. Surfactants on SION cores may act as a carbon source and become amorphous carbon during the annealing of SION@FSS so does magnetization value may slightly enhanced. Due to the thickness of the shell, magnetic moment may change. All the nanoparticles that were

synthesized based on SION@FSS were dragged by a small handheld magnet and were redispersed easily by shaking the vials after withdrawing the magnet.

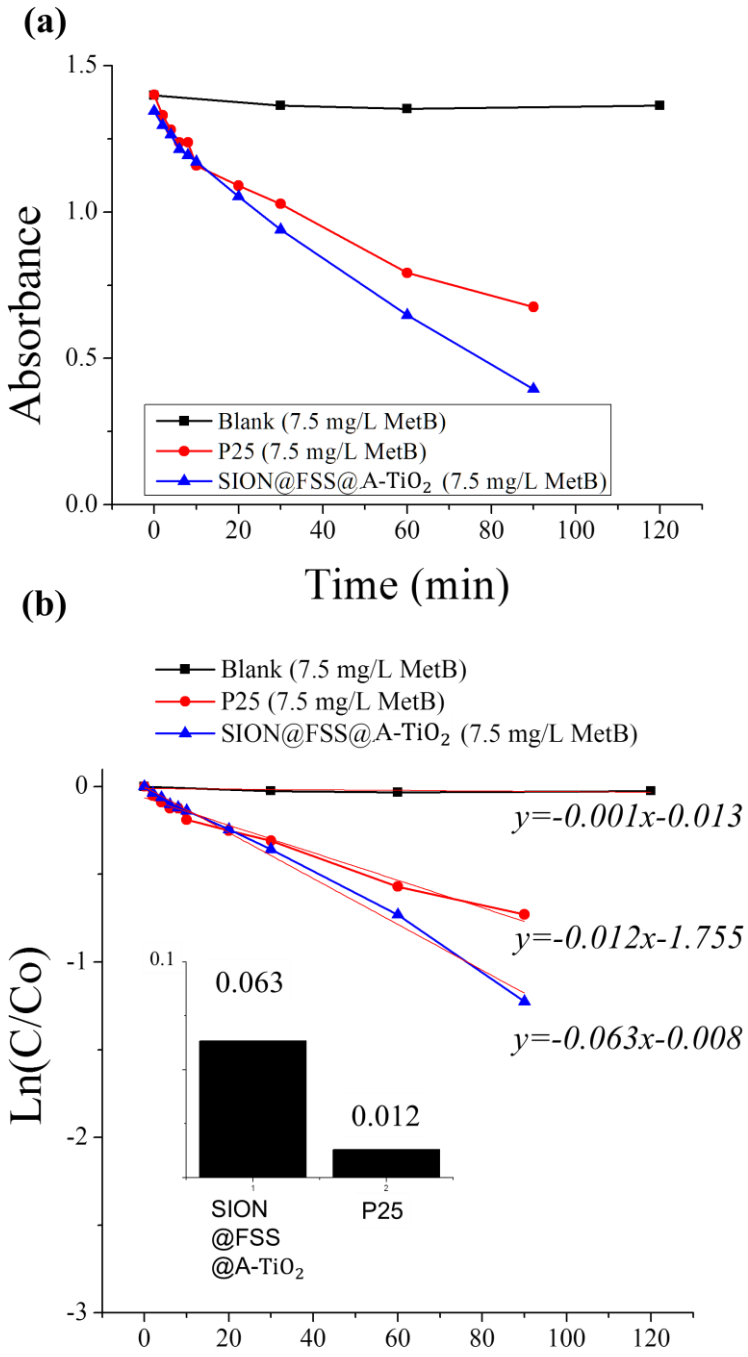

Figure 14. Degradation test with MetB solution (7.5 mg/L) and SION@FSS@A-TiO_2 compared to that with commercial P25. Absorbance vs. time (a) data was linear fitted (b) to compare rate constants (inset).

Finally, the catalytic effect of the anatase TiO_2 decorated on the particle surface is evaluated (Error! Reference source not found.), after reaching the absorption-desorption equilibrium after 2hr. MetB solution was purified using UV-illuminated catalyst

nanoparticles, SION@FSS@A-TiO_2. With the aid of SION@FSS@A-TiO_2, 3 mg/L of dye molecules were degraded before 3 h of UV-irradiation. SION@FSS@A-TiO_2 shows much higher dye decomposition rate than same amount of commercial P25 TiO_2 nanoparticles (Error! Reference source not found. (b), (c)). Since a considerable amount of non-catalytic materials are included in the mass of SION@FSS@A-TiO_2, rate constant in **Figure 14** might be higher for the reaction with catalysts, SION@FSS@A-TiO_2. Considering the very low first-order rate constant of anatase TiO_2 nanoparticles and thin film made in a similar manner without magnetic core and silica supports, the synthesis and the use of SION@FSS@A- TiO_2 may enhance the photocatalytic effect. Finally, the nanoparticles were reused after the degradation. The recycled SION@FSS@A-TiO_2 shows less catalyst deterioration after the repeated trials while retaining its structure at the end of the degradation trials. The removal time and concentration of degraded MetB dye is compared with other magnetically recollectable nanocomposites with TiO_2 nanoparticles. From the results, SION@FSS@A-TiO_2 show comparable degradation performance while considering the lamp intensity and amount of catalysts used.

Conclusions and Future Work

We have demonstrated that raspberry shaped magnetite nanostructures are very interesting and even key elements to fabricate flexible materials with low dielectric loss, high permittivity and permeability values at radio frequencies (1 MHz- 1 GHz). The permeability values achieved by composites made from collectively assembled corona magnetite nanoparticles are significantly higher than the existing magnetite-polymer composites and magnetite-PDMS composites. Additionally, the composites prepared with collectively assembled corona magnetite nanoparticles exhibit an extraordinary magnetic resonance, which changes with the particle size of magnetite nanoparticles. In contrast to these interesting and promising properties of the composites, the composites have high dielectric loss, which can be addressed easily by introducing an insulating layer around the magnetite nanoparticles. We believe such composites could be utilized for high-bandwidth radio frequency antennas as the dielectric loss values are further decreased.

We are currently aiming to identify the origin of the magnetic resonance by characterizing the material in a broader spectrum. Currently synthesis is performed to modulate the nanograin size or to dope the nanostructures with cobalt or manganese or nickel or zinc to modulate the magnetic properties. First experiments with cobalt showed that although similar saturation magnetizations have been obtained, the coercivity is larger as shown in the figure below. Other approaches would be to coat them with carboneous materials or silica or gold in collaboration with Dr Yuanzhe Piao.

Remarks : Prof Peter Kofinas has performed courses at Strasbourg (12h eq TD) as invited professor since 2014. Dr Yuanzhe Piao,Pr. Peter Kofinas and Pr S. Begin will co-organize together a symposium to the EMRS spring meeting 2017 entitled : Novel multifunctional nanomaterials for energy, sensing, electronic, and detection technologies.

Fe_3O_4

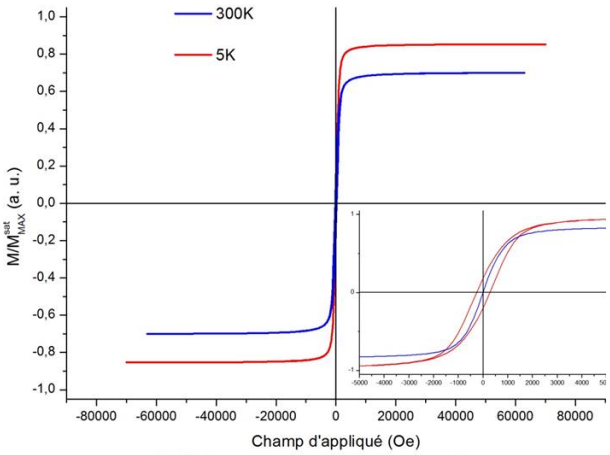

$M_S^{5K} = 86\ emu.g^{-1}$

$H_C^{5K} = 300\ Oe$

$Co_{0,08}Fe_{0,30}O_{0,62}$

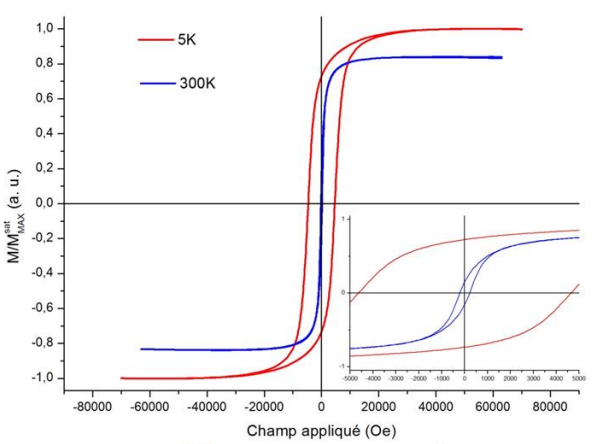

$M_S^{5K} = 80\ emu.g^{-1}$

$H_C^{5K} = 4600\ Oe$